How to use *DIALS* to process chemical crystallography 3D ED rotation data from pixel array detectors

Angelina Vypritskaia,[a] Xiaodong Zou,[a] Taimin Yang[a] and David Geoffrey Waterman[b]*

[a]Department of Materials and Environmental Chemistry, Stockholm University, Stockholm SE-106, Sweden, and [b]Research Complex at Harwell, UKRI–STFC Rutherford Appleton Laboratory, Harwell, Didcot, Oxfordshire, OX11 0FA, England, United Kingdom. *Correspondence e-mail: david.waterman@stfc.ac.uk

The *DIALS* package provides a set of tools for crystallographic data processing. The open-source nature of the project, and a flexible interface in which individual command-line programs each have a dedicated job, have enabled the adaptation of *DIALS* to a wide range of experiment types, including electron diffraction. Here we present detailed instructions for the use of *DIALS* to process chemical crystallography diffraction data from continuous rotation electron diffraction experiments. We demonstrate processing and structure solution from three different samples from three different instruments, including two commercial instruments dedicated to electron diffraction. Each instrument has a pixel array detector, allowing low-noise data to be obtained, resulting in high quality structures. Various new features were added to *DIALS* to simplify the workflow for these use cases. These are described in detail, along with useful program options for electron diffraction work.

1. Introduction

Electron crystallography has rapidly evolved over the past decade due to the development of 3D acquisition and electron diffraction data analysis protocols (Gemmi *et al.*, 2019). These advancements enable us to study the structure of materials with enhanced data quality and acquisition speed, which has been proved by the successful determination of various structures from minerals (Gemmi *et al.*, 2019), small organic molecules (Andrusenko & Gemmi, 2022), zeolites (Cho *et al.*, 2023) and metal–organic frameworks (Samperisi *et al.*, 2022; Huang *et al.*, 2021) to proteins (Clabbers & Xu, 2021).

Software development has also been crucial in supporting these new techniques, by providing robust data processing. *DIALS* (Winter *et al.*, 2018), originally developed for X-ray crystallography data processing, was later extended to work with electron diffraction data (Clabbers *et al.*, 2018), with an aim to provide unified software for crystallographic data processing. *DIALS* is freely available for download from https://dials.github.io/ under the terms of the BSD-3 license. Linux and Mac packages are provided. Additionally, *CCP4* (Agirre *et al.*, 2023) and *conda-forge* provide builds for Windows. The *DIALS* package consists of a suite of command-line programs, each of which performs a discrete step of data processing. In X-ray crystallography, where comprehensive metadata are usually associated with the image data, data processing may be achieved with simple commands that mainly use program defaults (the following is based on the X-ray small-molecule tutorial at the *DIALS* website):
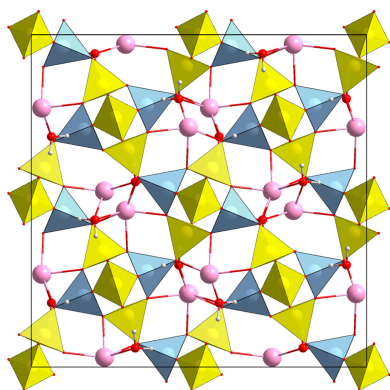
```
dials.import ../data/*.cbf
dials.find_spots imported.expt
dials.index imported.expt strong.refl\
    space_group=P222
dials.refine indexed.expt indexed.refl
dials.integrate refined.expt refined.refl
dials.symmetry integrated.expt integrated.refl
dials.scale symmetrized.expt symmetrized.refl
dials.export scaled.expt scaled.refl\
    format=shelx composition=CHNOS
```

In our research, we examine the processing of 3D electron diffraction (3D ED) data collected in three different setups: continuous rotational electron diffraction with calibration images (cRED) collected on an electron microscope at Stockholm University, data collected on a Rigaku Synergy-ED instrument at the UK National Electron Diffraction Facility and data from an Eldico ED-1 diffractometer at the Eldico Customer Experience Center in Basel. Each configuration has its unique benefits and challenges for collecting and analyzing data. We describe how *DIALS* is applied and adapted for each experimental scenario. We have included additional functionalities in *DIALS* according to the requirements encountered during our investigations. The new features have made the data processing workflow more efficient while maintaining *DIALS* as a reliable tool for electron crystallography analysis. The examples are based on publicly-available data, and we provide example *DIALS* processing scripts with detailed explanations of program parameters. This enables users to follow along and reproduce the results shown in the article. All data processing results shown were produced with *DIALS* Version 3.21.1, which contains the new features introduced to improve the handling of electron diffraction data.

2. cRED data

The development of fast read-out electron detectors, such as Timepix (van Genderen *et al.*, 2016), made it possible to collect electron diffraction data continuously, leading to the development of continuous rotational electron diffraction (cRED) (Cichocka *et al.*, 2018), also known as MicroED (Shi *et al.*, 2013). In a cRED experiment, the goniometer continuously rotates at a constant speed while the diffraction patterns are recorded over a certain exposure time. cRED allows faster data collection and more complete sampling of reciprocal space than stepwise tilt data collection, making it particularly useful for investigating radiation-sensitive materials, and it has been used successfully for studying various inorganic and organic samples and proteins, including a number of zeolites, MOFs and pharmaceuticals. The only hardware requirement for cRED data collection is a transmission electron microscope with a suitably high-quality single tilt sample holder and a camera. Merging several 3D ED data sets allows completeness to be increased (Ge *et al.*, 2021) and overall data quality to be improved (Xu *et al.*, 2018).

2.1. Electron nanocrystallography (NanED) Round Robin samples

NanED (https://naned.eu/) is a collaborative training program funded by the EU, aimed at training a new generation of electron crystallographers. This is intended to make it easier for electron diffraction methods to become widely accepted and used across academic and industrial environments.

Within the framework of the NanED project, the Round Robin deliverable was set up with two main goals: to train new researchers in 3D ED techniques using well-known samples and to compare results across different labs using a variety of microscopes and analysis methods (Gemmi *et al.*, 2023). As an example, we selected one of the Round Robin samples, natrolite, a mineral from a zeolite family, containing vertex-sharing TO_4 tetrahedra (T = Si or Al).

Crystals of the natrolite sample were crushed in an agate mortar. The powder was dispersed in ethanol and ultra-sonicated for 3 min. A drop of the suspension was placed on a copper grid with lacey carbon film. Data collection was performed at room temperature.

cRED data of the natrolite crystals were collected on a JEM-2100 LaB_6 microscope, with an accelerating voltage of 200 kV. A Timepix hybrid pixel detector and the *Instamatic* software (Cichocka *et al.*, 2018) were used for data collection. The resulting data sets consist of SMV format images. During data collection using *Instamatic*, every *n*th diffraction pattern is defocused (usually *n* equals 10 or 20) to track the crystal during rotation. The beam diameter was around 700 nm, and if the crystal was seen to move away from the beam centre this was adjusted by movement of the sample stage. This prevents the loss of the crystal due to crystal movement and allows data collection with large rotation ranges (Cichocka *et al.*, 2018). For the four data sets investigated here, the tilt per image ranged from 0.2296 to 0.2318°, and the total tilt ranged from 90.24 to 118.91°. Beam centre drift of a few pixels was evident over the course of data collection. However, diffraction patterns were not centred as the drift was tolerated in data processing.

2.2. Data processing

The *DIALS* commands used to integrate the natrolite data sets were similar in each case. For illustration, commands for processing a single natrolite data set within a *BASH* shell on a Linux computer are reproduced here.

```
dials.import "$NATROLITE_DATA"/Data1/SMV/data/*.img\
    geometry.goniometer.axis=-0.6204,-0.7843,0.0000\
    panel.gain=2.9
dials.generate_mask imported.expt\
    untrusted.rectangle=0,516,255,261\
    untrusted.rectangle=255,261,0,516
dials.apply_mask imported.expt mask=pixels.mask
dials.find_spots masked.expt\
    exclude_images_multiple=20\
    d_max=10 d_min=0.6 gain=0.5
dials.index masked.expt strong.refl\
```

```
      detector.fix=distance space_group=F222
dials.reindex indexed.expt indexed.refl\
    change_of_basis_op=b,c,a space_group=Fdd2
dials.refine reindexed.expt reindexed.refl\
    detector.fix=distance
dials.integrate refined.expt refined.refl\
    prediction.d_min=0.6\
    exclude_images_multiple=20
```

This assumes that the path to the parent directory containing the natrolite data sets is given by the variable `NATROLITE_DATA`. Key points regarding the behaviour of *DIALS* during the execution of these commands are explained in the following sections.

2.2.1. Determining the rotation axis

The SMV format has no robust metadata standard and diffraction geometry metadata is typically incomplete (Waterman *et al.*, 2023). While the beam centre is written to the image header by *Instamatic*, and is read by *DIALS*, there is no header entry to represent the orientation of the rotation axis in the image. The *dxtbx* format class (Parkhurst *et al.*, 2014) used to read the SMV images from this microscope assumes a default orientation, which was determined some years ago. During processing of the Round Robin data sets it was discovered that the rotation axis now differs slightly from this default.

An algorithm for determining the rotation axis orientation from diffraction data has been reported by Kolb *et al.* (2009), and since then has been adopted by other packages, such as *PETS2* (Palatinus *et al.*, 2019) and *edtools* (Cichocka *et al.*, 2018). The program *dials.find_rotation_axis* also implements this algorithm and is a direct adaptation of the open source *edtools* version. The algorithm is effective in the case of good quality spot-finding results from a single crystal. If a large number of noise peaks are found as spots, then the algorithm may fail to identify the correct orientation. We ran *dials.find_rotation_axis* on several of the Round Robin data sets, then set the same consensus value *via* the `geometry.goniometer.axis=` option of *dials.import* for all further processing. For any one data set, the *dials.find_rotation_axis* command was run after spot-finding as follows:

```
dials.find_rotation_axis masked.expt strong.refl
```

2.2.2. Determining the detector gain

The Timepix detector is able to count events with energy higher than a user-defined threshold (van Genderen *et al.*, 2016). Due to scattering of high-energy electrons within the silicon sensor, charge spread beyond the point of incidence may result in counts within neighbouring pixels. The detector gain, defined as the number of detected counts per incident electron, is expected to be greater than 1 due to this charge sharing. The value of the gain is important for spot-finding, and for a realistic scale of the integrated intensity error estimates, $\sigma(I)$, before further modifications to the error model

are made in scaling. For a detector without a pedestal offset, the gain can be estimated by comparing the observed index of dispersion with the value 1.0, which is the expected value for a perfect counting detector. The program *dials.estimate_gain* performs this calculation within a local region of background scatter, but this method is known to underestimate the true gain for a detector with non-negligible point spread (Waterman & Evans, 2010; Clabbers *et al.*, 2018).

A reviewer of an earlier version of this article pointed out an alternative way to experimentally measure gain for a PAD. This method is rather direct and subject to fewer assumptions than approaches based on variance of the signal. Illumination of the detector with a very low dose allows identification of single electron impacts, which generally form clusters of a few pixels. In this context, the gain may be known as the 'event multiplicity', and is given by the average number of counts across correctly identified single electron impacts (Fernandez-Perez *et al.*, 2021). We collected low-dose images of 200 keV electrons from the Timepix detector with the software *SoPhy*, provided by Amsterdam Scientific Instruments. The smallest condenser aperture (10 µm) was used, and the spot size was 5, with magnification at 600 000× and 0.1 s frame exposure. An analysis of event clusters from 40 images resulted in the value 2.9 for the event multiplicity, which we then set at import using the `panel.gain=` parameter (see Section S1 in the supporting information for further details).

We found that the results from *dials.find_spots* using this higher gain estimate tended to omit weaker but clearly visible spots, as inspected with the *dials.image_viewer*. For this reason, we added the parameter `gain=0.5` to the *dials.find_spots* command. Here it acts as a multiplier for the panel gain set at import, so that the gain assumed by the spot-finding algorithm is 1.45 rather than 2.9. This increased the sensitivity of spot-finding, recovering some of the weaker spots. While the panel gain set at import persists throughout the steps of data processing with *DIALS*, the adjustment performed for spot-finding affects that step only.

2.2.3. Masking the central cross

The Timepix quad detector consists of four 256×256 pixel chips, each of which has an outer border composed of wider pixels (van Genderen *et al.*, 2016). The area where the chips join forms a central cross in the image of two pixels width, with greater intensity values than the surrounding pixels due to their larger physical size. After conversion by the *Instamatic* software, the overall image size is expanded to 516×516 pixels to account for the size of the central cross region. The intensity of pixels within the cross is adjusted to the scale of the surrounding pixels; however, the profiles of reflections recorded in the cross are affected and are not well modelled by reflection profiles recorded elsewhere on the detector. For this reason, for programs like *DIALS* that do integration by profile fitting, it is not recommended to use the pixels in this cross. For the cRED processing presented here, this was achieved by explicitly masking those pixels using the *dials.generate_mask* and *dials.apply_mask* commands. These commands have been

left in the script above as an example; however, for simplicity, this mask has now been added to the format class used to read the images.

2.2.4. Excluding crystal tracking images

DIALS can exclude images from spot-finding, integration and scaling, using a consistent syntax given by `exclude_images=exp:start:stop`, where `exp` gives the experiment number, and `start` and `stop` give the inclusive range of images to exclude from consideration. Multiple ranges can be provided in a single definition by comma-separated values, and multiple definitions of the parameter will be combined. While flexible, this syntax was found to be inconvenient for scripting the processing of cRED data. To simplify the interface, we added the parameter `exclude_images_multiple=n`, where, for example, $n = 20$. This is automatically expanded into the appropriate image exclusion definition to regularly exclude each image number exactly divisible by n within the image range of the data set. The collection of crystal tracking images is a feature provided by *Instamatic*, so the new parameter makes it easier to work with *DIALS* on data collected by *Instamatic* on any instrument it supports.

Image exclusions defined in spot-finding act as a mask, setting all pixels to 'invalid' on the excluded images. Diffraction spots that are interrupted by a tracking image may be found within two separate spot shoeboxes (before and after the tracking image). Typically, *dials.index* will only index one of the two in these cases, leading to error in the centroid position and profile for that spot. Nevertheless, these effects are mitigated by the diffraction geometry refinement and profile modelling using data from the whole scan.

During integration, image exclusion also acts like a mask. For spots whose peak region is intersected by a tracking image, no summation integration intensity estimate is possible.
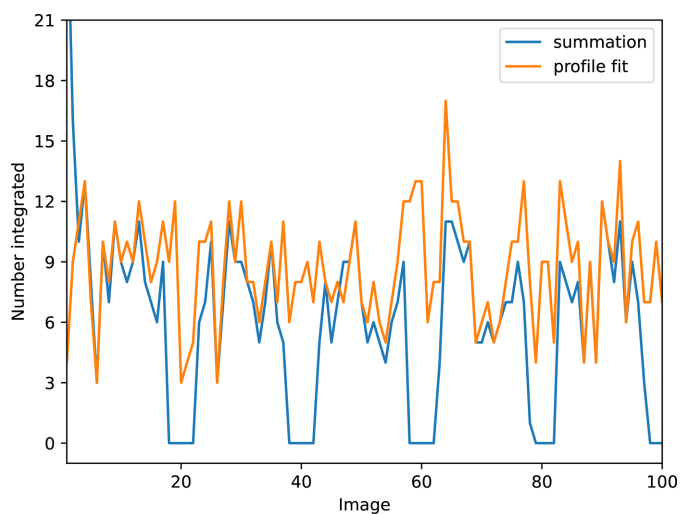

Figure 1
Comparison of the number of reflections integrated by either summation integration or profile fitting on each of the first 100 images of the first natrolite data set (Data1). Calibration image numbers are located at each multiple of 20.

Therefore, a plot of the number of summation integrated spots shows wide gaps around the calibration images, as shown by Fig. 1. Profile fitting is able to recover an intensity estimate even when the peak region contains some invalid pixels. This is controlled by the `valid_foreground_threshold` parameter for *dials.integrate*, which is set to 0.75 by default. Thus, as long as 75% of the pixels forming the diffraction spot are outside the excluded image, or not otherwise masked, then a profile fitting estimate will be recorded. Fig. 1 shows that the number of profile-fitted intensities drops at the tracking images, but not to zero. The overall number of profile-fitted intensities is about 50% higher than the number of summation integrated intensities for this data set.

This procedure was seen to work well for data sets we tried where every 20th image was a tracking image. In some cases where $n = 10$ instead we saw a failure in profile fitting because *dials.integrate* could not create a profile model. This occurred when the full extent of the observed rocking curve of strong reflections exceeded the spacing between tracking images. Thus, the spacing between these images should be chosen carefully based on the properties of the sample.

2.2.5. Indexing and refinement

The default 3D FFT indexing method of *DIALS* usually works well with these cRED data sets. Indexing success hinges on the quality of spot centroid data, and noise peaks may cause problems with basis vector determination. Pixel array detectors allow data collection without a beamstop and, unless there is an energy filter, this reveals a cone of significant background at low angle around the beam centre, caused by inelastic scatter of the direct beam. This typically leads to a spherical region around the centre of reciprocal space within which many noise peaks are found. The simplest way to avoid this and provide better data for indexing is to set a low resolution limit in Å, such as `d_max=10`, for *dials.find_spots*.

Unless a space group is provided, *dials.index* will return a triclinic solution. In this case, the space group for natrolite is known to be $Fdd2$ (Fig. 2). However, *dials.index* will return an orthorhombic solution by convention with $a < b < c$, whereas the correct solution has $c < a < b$. Rather than setting the space group to $Fdd2$ immediately, we first specified the subgroup $F222$ to ensure that the unit-cell refinement performed by *dials.index* was appropriately constrained. Once this solution was written out, the program *dials.reindex* was used to change the basis and to set the correct space group.

In some cases with higher symmetry space groups, enforcing lattice constraints can lead to excessively high root-mean-square deviations between predicted and observed spot positions, negatively affecting integrated data quality. This can occur if unmodelled distortions from post-sample lenses (Brázda *et al.*, 2022), or other deviations from the refined diffraction geometry, are present. In such cases, it can be useful to process data using the triclinic solution, in which the unmodelled geometry errors may be transferred, to some extent, to errors in the unit-cell parameters. After integration, automatic determination of symmetry may be performed

using tools such as *dials.symmetry* or *dials.cosym* (Gildea & Winter, 2018), to ensure scaling is performed with the correct Laue class. In the experience of the authors, however, much care must be taken when using the *DIALS* symmetry-determination tools with 3D ED data. The generally higher errors on intensities due to effects such as multiple scattering in such data as compared to X-ray data can lead to incorrect results.

Simultaneous refinement of the detector distance and the unit-cell parameters is not usually possible for 3D ED data unless a restraint is applied (Clabbers *et al.*, 2018). Here we simply fixed the detector distance using the `detector. fix=distance` parameter, for the *dials.index* and *dials.refine* commands, both of which perform geometry refinement. This implies that errors in the calibrated effective detector distance will be expressed as errors in the refined unit-cell lengths. It may be possible to correct such errors after structure solution during model refinement (Gruene *et al.*, 2022).

After refinement of a static model for the experiment, *dials.refine* performs a scan-varying refinement, in which parameters are allowed to vary as a smoothed function of position within the rotation scan (Waterman *et al.*, 2016; Clabbers *et al.*, 2018). The default behaviour is to allow the crystal orientation and unit-cell parameters to vary in this way, while other parameters, such as the beam direction, and the detector position and orientation are refined to static values. In the case of 3D ED data collection from nanocrystals using a selected area aperture, the beam is generally larger than the sample, ensuring there is no apparent unit-cell variation due to the sampling of different mosaic blocks during data collection. Changes to the unit-cell values due to radiation damage may still be present, but for the natrolite data these are expected to be small. Other errors, such as drift of the direct beam and distortion in the diffraction patterns caused by post-sample lenses, were not directly accounted for here; however, their effects may be partially compensated for by the scan-varying
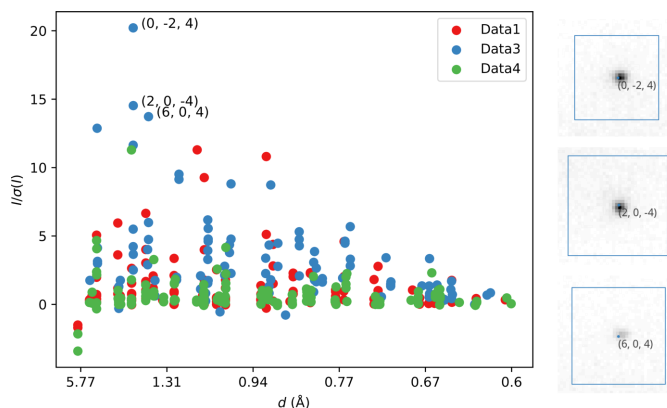

Figure 2
$I/\sigma(I)$ *versus* resolution for 364 reflections from the scaled natrolite data sets that should be systematically absent in the space group *Fdd*2 under the kinematic approximation. The points are coloured according to which of the three crystals they come from. A few reflections from each crystal show significant violation of their expected absence. On the right, images from the *dials.image_viewer* of the three spots with highest $I/\sigma(I)$ are shown, clearly indicating that these violations are present in the data and are not an artefact of data processing.

refinement of crystal parameters. There was a small improvement in merging statistics seen by allowing the unit cell to vary smoothly, so we used this model for further processing.

2.2.6. Determining the best overall unit cell

The unit cells determined by *dials.refine* are based on refinement against the indexed strong spot centroids, without background subtraction. A more precise unit-cell refinement can be performed after integration using the recalculated integrated spot centroids, including background subtraction. The program *dials.two_theta_refine* performs this analysis. By using a target function based on the reflection 2θ scattering angles rather than the position of reflection impacts, the data from multiple crystals at different orientations are combined to produce a single best (in a least-squares sense) cell for all data sets. The command used to do this for a combination of three of the natrolite data sets was

```
dials.two_theta_refine\
    "$NATROLITE_PROC"/Data1/integrated.{expt,refl}\
    "$NATROLITE_PROC"/Data3/integrated.{expt,refl}\
    "$NATROLITE_PROC"/Data4/integrated.{expt,refl}
```

This assumes that the processing of each data set was performed in its own directory, under a common parent directory, the path to which is stored in the variable `NATROLITE_PROC`. The command produced the file refined_cell.expt, in which the single unit cell with standard uncertainties was given as $a = 18.640$ (9), $b = 18.788$ (4) and $c = 6.8419$ (16) Å.

2.2.7. Scaling multiple data sets

Combining multiple data sets may be important in cRED in order to increase completeness and to help average out the typically high errors (compared to X-ray crystallography) (Xu *et al.*, 2018; Ge *et al.*, 2021). As long as the integrated data sets are consistently indexed, then they can be jointly-scaled by *dials.scale* (Beilsten-Edmands *et al.*, 2020). First we tried joint scaling of all four natrolite data sets. Inspection of the plot of scale factor against batch reported in the dials.scale.html file indicated that the second data set, `Data2`, comprised considerably weaker diffraction intensities than the other data sets. Exclusion of this data set produced better merging statistics and a lower refinement R_1 value. Therefore, we discarded that data set and scaled the three remaining natrolite data sets using the command given here, run in the same directory as the refined_cell.expt file produced by *dials.two_theta_refine*.

```
dials.scale refined_cell.expt\
    "$NATROLITE_PROC"/Data1/integrated.refl\
    "$NATROLITE_PROC"/Data3/integrated.refl\
    "$NATROLITE_PROC"/Data4/integrated.refl\
    merging.nbins=10\
    d_min=0.61
dials.export scaled.expt scaled.refl\
```

```
format=shelx\
composition="Si Al Na O H"
```

The first option passed to *dials.scale* after the sequence of integrated data sets is merging.nbins=10. This option does not change the behaviour of the scaling algorithm, but just sets the number of bins used for reporting merging statistics. The default value is 20, but for small unit cells this can lead to noisy values for the merging statistics, as there are relatively few reflections in each bin. We found that reducing the value to 10 produced more reasonable values for merging statistics in the inner and outer resolution shells, reported in tables such as Table 1.

The second option passed to *dials.scale*, d_min=0.61, sets the high resolution limit for reflections included in scaling and merging.

2.3. Structure solution and refinement

After scaling, the unmerged data were exported using *dials.export*, specifying the composition to produce dials.ins and dials.hkl files suitable for immediate use by *SHELXT* (Sheldrick, 2015a). Structure solution was straightforward with the data processed as described; however, it is worth raising a note of caution. Prior to estimating the detector gain using the method described in Section 2.2.2, we used a lower value for the detector gain, and in this case found that the structure could be solved by *SHELXT* Version 2014/5, but Version 2018/2 failed to produce a solution. A feature introduced in Version 2018/2 is the rejection of space groups where systematic absences have a mean $I/\sigma(I) > 5$ (as noted at https://shelx.uni-goettingen.de/changes.php). *DIALS* always integrates reflections that should be absent due to screw axes or glide planes given the supposed space group, and we suspected that systematic absence violation was the cause of the failure to solve the structure in this case.
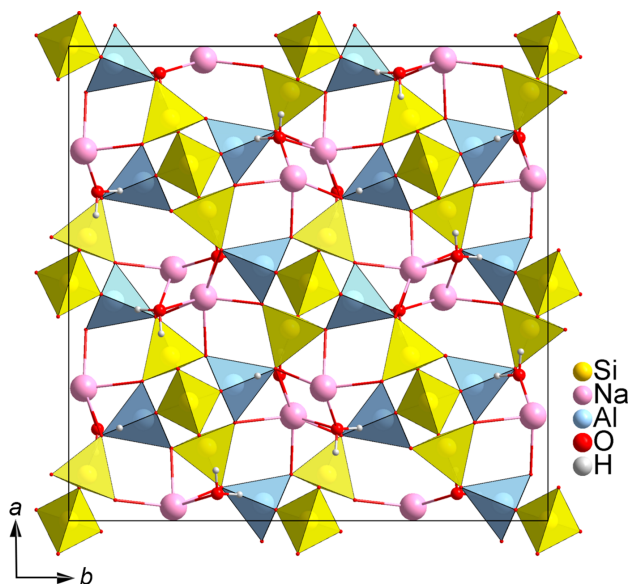

Figure 3
The crystal structure of natrolite along the [001] direction.

Table 1
Statistics for joint scaling of three natrolite data sets.

Crystallographic data and merging statistics			
Molecular formula	$Na_2Al_2Si_3O_{10}\cdot 2H_2O$		
Space group	*Fdd*2		
a, b, c (Å)	18.640 (9), 18.788 (4), 6.8419 (16)		
	Overall	Low	High
High resolution limit	0.61	1.31	0.61
Low resolution limit	6.62	6.62	0.63
Completeness (%)	95.7	100	71.1
Multiplicity	7.2	8.3	3.2
I/σ	13.0	39.3	2.2
$R_{meas}(I)$	0.198	0.115	0.515
$R_{pim}(I)$	0.067	0.039	0.261
$CC_{1/2}$	0.991	0.994	0.474
Total observations	10211	1395	345
Total unique	1410	168	108
Kinematical refinement			
Reflections		All	$[I > 2\sigma(I)]$
Independent reflections		2469	1948
R_1		0.1681	0.1448
wR_2		0.3767	0.3557
Goof		1.175	

Once the gain was better estimated by the event multiplicity method, the structure was solved by either version of *SHELXT*. Nevertheless, an analysis of the systematic absences shown in Fig. 2 revealed numerous reflections that are expected to be absent in fact still had significant diffraction intensity. These violations of the reflection conditions are expected in 3D ED due to multiple scattering. Although increasing the gain value, which led to an increase in the sigma estimates for reflections, was enough to avoid failure in *SHELXT* in this case, it is worth being aware of this issue, particularly in cases where crystals are relatively thick, or the sigma estimates on intensities may be severely underestimated. The error model refined by *dials.scale* defaults to a physical model similar to that in *AIMLESS* (Evans & Murshudov, 2013), which works well for synchrotron X-ray data sets. In general, we suspect that for 3D ED data sets the error estimates from *DIALS* may be too small. The issue of optimal error modelling for 3D ED data has been addressed by Khouchen *et al.* (2023). This model has not yet been assessed within *DIALS*.

The structure was solved using the dual-space method with *SHELXT* and least-squares refinement was performed using *SHELXL* (Sheldrick, 2015b). All atoms were refined anisotropically. The extinction parameter EXTI was applied in the refinement. This was required to partially compensate for the dynamical effects on the intensities, thereby avoiding anisotropic displacement parameters for some atoms from becoming non-positive definite (NPD), and to stabilize the positions of H atoms, which were not fixed. The structure is shown in Fig. 3.

2.3.1. Investigation of reindexing possibilities

Natrolite is pseudo-tetragonal with $a \approx b$. Errors on observed unit-cell dimensions are generally higher from 3D ED data on a standard Transmission Electron Microscope (TEM) than from an X-ray diffractometer. We considered the possi-

bility that individual data sets may have been misindexed, swapping the *a* and *b* axes. In many cases such a situation would be associated with poor merging statistics. Programs such as *dials.symmetry* allow automatic reindexing of data sets to form a consistent set. However, for natrolite, the effect of misindexing on the diffraction intensities is subtle. Indeed, the program combines the three data sets assuming tetragonal symmetry. Scaling under these constraints produced merging statistics that are similar [overall $R_{meas}(I) = 0.235$ compared to 0.198 from the run in *Fdd*2]. Subsequent phasing by *SHELXT* gave a solution in the space group $I\bar{4}2d$, which is the space group for gonnardite, a related mineral with a disordered natrolite framework (Artioli & Galli, 1999). We could not use *dials.symmetry* to automatically determine the correct reindexing possibilities for orthorhombic natrolite; however, with just three data sets to consider, and without treating one data set as a reference, there are only eight possible combinations in which between zero and three data sets are reindexed to swap the similar length axes. For any particular data set, that was achieved by replacing the *dials.reindex* command in the listing in Section 2.2 with the following command, and otherwise processing identically:

```
dials.reindex indexed.expt indexed.refl\
    change_of_basis_op=c,b,-a space_group=Fdd2
```

For all eight runs, *SHELXT* found a solution in *Fdd*2. An initial refinement of the solutions showed clearly better results for the run in which no reindexing was performed, therefore the initial assignment of axes was found to be correct. Refinement results are presented in Table S4.

3. Rigaku Synergy-ED data

Data sets were collected at the UK National Electron Diffraction Facility (NEDF) site at the University of Southampton. The facility is equipped with Rigaku XtaLAB Synergy-ED instruments, combining a JEOL JSM-2300ED electron source optimized for diffraction studies at 200 kV, with a Rigaku HyPix-ED hybrid pixel array detector. We chose nine data sets of L-histidine chloride monohydrate collected at a temperature of 175 K by NEDF staff as our example of processing with *DIALS*. Two data sets were collected with a tilt per image of 0.25°, while the remaining five used 0.2° per image. Total tilt ranged from 112 to 126.4°.

3.1. Data processing

The *DIALS* commands used to integrate one of the histidine data sets are as follows:

```
dials.import\
    "$HISTIDINE_DATA"/exp_705/frames/*.rodhypix\
    panel.gain=2.9\
    geometry.goniometer.axes=0,-1,0,\
0,-0.642788,0.766044,\
0.050593,-0.99872,0\
```

```
    image_range=1,484
dials.find_spots imported.expt d_max=10 gain=0.5
dials.index imported.expt strong.refl\
    detector.fix=distance space_group=P212121\
    max_lattices=2 minimum_angular_separation=1
dials.refine indexed.expt indexed.refl\
    detector.fix=distance
dials.integrate refined.expt refined.refl\
    prediction.d_min=0.6
```

The path to the parent directory containing the histidine data sets is given by the variable HISTIDINE_DATA.

3.1.1. Importing the data set

The Rigaku Oxford Diffraction file format contains a comprehensive specification of diffraction geometry as metadata. The *dxtbx* format class used to read these images does not read all metadata items, but extracts enough from the header to create a model for the experiment. The gain is assumed to be equal to 2.9 and is set at import. This value was determined experimentally using low dose imaging to identify single electron impacts (Robert Bücker, personal communication). As with the natrolite example, we found that the sensitivity of spot-finding was too low using this gain value, so we passed the option gain=0.5 to *dials.find_spots* to ensure weak spots were located.

One complication with images from the Rigaku diffractometer is that the incremental image number that forms part of the filename is not zero-padded. For example, the 496 images of the exp_705 data set begin with file exp_705_ 1_1.rodhypix and end with exp_705_1_496. rodhypix. This is counter to the typical scheme used at synchrotron beamlines and other facilities, in which the final number has a fixed width, such as 0001 to 0496. Initially *DIALS* could not interpret this image filename template as a contiguous range of images, and we had to rename images to conform to a zero-padded template. During the course of this work, we added the ability to read filename templates with non-zero-padded image numbers.

The orientation of the rotation axis is read from the image metadata, which in this case locates it exactly antiparallel to the *y* axis. In fact, runs of *dials.find_rotation_axis* on each data set gave a corrected axis orientation about 2.9° from this nominal orientation. We found that it was not necessary to correct the orientation in order to successfully index each of the example data sets; however, in general, it is best to determine the rotation axis using good data sets and then set it to process all other data sets where it should be the same. The Rigaku Oxford Diffraction format contains a description for a multi-axis goniometer, even though for the Synergy-ED instrument only a single axis is used. In order to set the corrected axis at import, we used the geometry.goniometer.axes option to set nine values, three for each axis in order from the sample to the goniometer base. These values were taken from the *dials.find_rotation_axis* log file for one of the runs.

These data sets contain some images at the extremes of the tilt range where part of the diffraction pattern is shadowed by

the sample holder. We identified these images by inspection using the *dials.image_viewer* and then chose to exclude them from import using the `image_range` parameter.

3.1.2. Indexing multiple lattices

During the initial processing of these data sets, we found that the percentage of indexed spots was generally high, though somewhat lower for three of the data sets: `exp_705`, `exp_710` and `exp_712`. Explorations with *dials.reciprocal_lattice_viewer* revealed the presence of more than one lattice in these cases. We indexed the second lattice for `exp_705` by providing the option `max_lattices=2` to *dials.index*, as shown in the example processing commands. This option causes the program to attempt to index again from the unindexed spots remaining after the first lattice is found. When an additional lattice is found, *dials.index* will reject it if it is in too similar an orientation to any previously-accepted lattice, under the control of the `minimum_angular_separation` parameter. The default value for this is $5°$, which for the example data set `exp_705` resulted in rejection of the second lattice, which was rotated by just $3.3°$ from the first. Reducing the value to `minimum_angular_separation=1` ensured that the second lattice was retained. Single lattice indexing assigned 59% of the found spots to one crystal model, while two lattice indexing assigned 52% of spots to the first lattice and a further 42% of spots to the second lattice. The decrease in proportion of spots assigned to the first lattice indicates the reassignment of spots that are more appropriately indexed by the second lattice. Finding the second lattice and reassigning those spots therefore improves the indexing results for the first lattice too.

Processing both lattices from `exp_705` improved the overall merged data set, whereas conversely the additional lattices found in `exp_710` and `exp_712` diffracted weakly and reduced the overall quality of merged data. Therefore, we integrated only the major lattice in these two cases.

When there are multiple lattices in a single data set, it is likely that some diffraction spots will overlap, adding error to integrated intensities. This is particularly the case for lower resolution reflections of closely-aligned crystals. If all lattices that are present are successfully indexed, the information is available in principle to detect the spots that overlap and either reject their intensities, or attempt to deconvolute them. Unfortunately, *dials.integrate* does not offer this facility yet. We investigated overlapped reflections in this case and found that they were also not removed as outliers by *dials.scale* (see supplementary Section S2). Nevertheless, we encountered no difficulties in solving and refining the structure, so may conclude that errors from overlaps in `exp_705` are tolerable in this case.

3.1.3. Combining data sets, scaling and export

An overall unit cell was refined against all of the integrated data sets with the following command:

```
dials.two_theta_refine\
    "$HISTIDINE_PROC"/exp_705/integrated.{expt,refl}\
```

```
    "$HISTIDINE_PROC"/exp_706/integrated.{expt,refl}\
    "$HISTIDINE_PROC"/exp_707/integrated.{expt,refl}\
    "$HISTIDINE_PROC"/exp_708/integrated.{expt,refl}\
    "$HISTIDINE_PROC"/exp_710/integrated.{expt,refl}\
    "$HISTIDINE_PROC"/exp_711/integrated.{expt,refl}\
    "$HISTIDINE_PROC"/exp_712/integrated.{expt,refl}\
    "$HISTIDINE_PROC"/exp_713/integrated.{expt,refl}\
    "$HISTIDINE_PROC"/exp_715/integrated.{expt,refl}
```

Here we assume that the processing of each data set was performed in its own directory, under a common parent directory, and we have provided the path to that parent directory in the `HISTIDINE_PROC` variable. The unit cell with standard uncertainties was determined to be $a = 6.7936 (3)$, $b = 8.8294 (4)$ and $c = 15.1621 (10)$ Å, with the space group $P2_12_12_1$. This unit cell was carried through to the exported *SHELX* .ins file and later used for model refinement. The commands used to scale and export the data were:

```
dials.scale\
    refined_cell.expt\
    "$HISTIDINE_PROC"/exp_705/integrated.refl\
    "$HISTIDINE_PROC"/exp_706/integrated.refl\
    "$HISTIDINE_PROC"/exp_707/integrated.refl\
    "$HISTIDINE_PROC"/exp_708/integrated.refl\
    "$HISTIDINE_PROC"/exp_710/integrated.refl\
    "$HISTIDINE_PROC"/exp_711/integrated.refl\
    "$HISTIDINE_PROC"/exp_712/integrated.refl\
    "$HISTIDINE_PROC"/exp_713/integrated.refl\
    "$HISTIDINE_PROC"/exp_715/integrated.refl\
    merging.nbins=10\
    d_min=0.64
dials.export scaled.expt scaled.refl\
    format=shelx composition="C H N O Cl"
```

Merging statistics from the *dials.scale* run with options as above are given in Table 2.

3.2. Structure solution and refinement

The structure was solved by the dual-space method using *SHELXT* and least-squares refinement was performed using *SHELXL*. All non-H atoms were refined anisotropically. The extinction parameter EXTI was applied in the refinement to stabilize the refinement of H-atom positions. It was possible to locate all H atoms during kinematical refinement from the Fourier difference map, as shown in Fig. 4. The last H atom was added after a refinement run after adding all other H atoms. Then H-atom ADPs were refined one atom at a time. Since the density peak for the last H atom was on the noise level and the N—H bond distance appeared to be very long (1.2 Å), the distance between these atoms was restrained. Table 2 summarizes the crystallographic data and refinement results and the structure is shown in Fig. 4.

3.2.1. Determining the absolute hand

Data for the best diffracting histidine crystal, `exp_715`, were exported as 'virtual frames' (Klar *et al.*, 2023) by

adopting the format pioneered by *PETS2*. The *DIALS* command used to do this was:

```
dials.export\
    "$HISTIDINE_PROC"/exp_715/integrated.{expt,refl}\
    format=pets n_merged=5 step=3
```

The `n_merged` parameter controls the number of real frames to merge in a virtual frame, while `step` selects the number of frames between each virtual frame. The step size is smaller than the number of frames to merge, so that virtual frames overlap. The output of this command is the file dials_dyn.cif_pets that can be passed to *JANA2020* for dynamical refinement, as detailed in Klar *et al.* (2023). By this procedure, the correct L-enantiomer was determined successfully as the one giving the smaller R value, with confidence as reported by the z-score, as calculated by *jana_tools* (Klar, 2023). These dynamical refinement results are summarized in Table 2.

4. Eldico ED-1 data

The Eldico ED-1 instrument is a dedicated electron diffractometer, with a high-precision goniometer and a horizontal layout, minimizing the sphere of confusion at the sample position (Simoncic *et al.*, 2023; Heidler *et al.*, 2019). The diffractometer has a 160 kV LaB_6 electron source and no post-sample lenses. This simple yet robust design avoids distortions in diffraction patterns that are otherwise common with 3D ED data (Brázda *et al.*, 2022), enabling accurate unit-cell determination. The trade-off is that it is not possible to alter the effective detector distance. For the current instrument, this means it is not possible to analyse samples with very large unit cells. For example, if a minimum spacing of four pixels between spot centres is required for successful data processing of a particular crystal, then at the detector distance of 578.3 mm used for the data sets we investigated, the maximum unit-cell dimension would be 55 Å. For crystals where spot size is increased due to factors such as high mosaicity, the minimum spacing between resolved spots may be larger, further limiting the maximum unit-cell dimension. Nevertheless, in principle, the design still permits adjustments of the mechanical detector distance, exactly as with an X-ray beamline.

For illustration of data processing, four data sets from crystals of 1,3,5-triphenylbenzene (TPB), collected at room temperature by Eldico staff, were chosen. Sample preparation and data collection details were the same as published previously in Simoncic *et al.* (2023). Each data set was collected with a tilt per image of 0.5° and total tilt ranged from 85 to 110°.

4.1. Data processing

The *DIALS* commands used to integrate each data set were equivalent. Here we show the script for one of the data sets,

Table 2
Statistics for joint scaling of nine histidine data sets.

Crystallographic data and merging statistics			
Molecular formula	$C_6H_{10}ClN_3O_2$		
Space group	$P2_12_12_1$		
a, b, c (Å)	6.795 (2), 8.824 (2), 15.149 (3)		
	Overall	Low	High
High resolution limit	0.64	1.38	0.64
Low resolution limit	8.83	8.83	0.66
Completeness (%)	100	100	100
Multiplicity	40.4	35.9	35.6
I/σ	13.9	53.0	1.8
$R_{meas}(I)$	0.430	0.231	1.946
$R_{pim}(I)$	0.065	0.037	0.333
$CC_{1/2}$	0.997	0.997	0.350
Total observations	85372	8826	7296
Total unique	2115	246	205
Kinematical refinement			
Reflections		All	$[I > 2\sigma(I)]$
Independent reflections		3641	2589
R_1		0.1484	0.1231
wR_2		0.3237	0.3132
Goof		1.126	
Dynamical refinement			
		L-His	D-His
R_1(all)		0.1904	0.2117
R_1(obs)		0.1269	0.1473
wR_2(all)		0.2677	0.2997
wR_2(obs)		0.2380	0.2696
z-score		5.1σ	

where the parent directory containing each data set directory is given by the variable `TPB_DATA`:

```
dials.import "$TPB_DATA"/03/*.cbf\
    panel.gain=1.6\
    geometry.goniometer.axis=-0.052336,0.99863,0
dials.find_spots imported.expt d_max=10
dials.index imported.expt strong.refl\
    detector.fix=distance space_group=P222
dials.refine indexed.expt indexed.refl\
    detector.fix=distance\
    crystal.unit_cell.force_static=True
dials.integrate refined.expt refined.refl\
    prediction.d_min=0.7
```

4.1.1. Importing the data set

Data from the ED-1 instrument was provided in miniCBF format, which is a relatively simple file format suitable for capturing diffraction geometry information from conventional rotation experiments with a single axis orthogonal to the beam direction. *DIALS* reads miniCBF format natively; nevertheless, we added a format class specific for the ED-1 instrument to the *dxtbx* library. This allowed us to set some specific defaults, ensuring an unpolarized electron beam model was created, and that the parallax and QE (Quantum Efficiency) corrections controlled by the detector model were disabled, as the form of these corrections in *DIALS* is appropriate only for X-ray data. The *DIALS* interpretation of these files places the rotation axis exactly along the y axis. In fact, runs of

dials.find_rotation_axis indicated that the true axis is about 3° offset from this. As the rotation axis is fixed and there are no post-sample lenses, this value can be considered a constant for the instrument. As for previous examples, we set the orientation of the axis explicitly as an option to the *dials.import* command.

The miniCBF images do not contain metadata giving the detector gain. We performed a similar analysis to that presented in Section 2.2.2 to estimate the gain to be 1.6. In contrast to the previous two examples, we found that spot-finding did not require an increase in sensitivity to capture weak spots. In fact, setting `gain=0.5` as an option to *dials.find_spots* in this case resulted in the algorithm being too sensitive, with many noise spots being found in addition to the Bragg peaks.

4.1.2. Further processing

The space group of TPB is $Pna2_1$, but it is unnecessary to set the exact space group for integration. What matters is that the Bravais lattice is correct. Here we ensured that by using the subgroup $P222$ to enforce orthorhombic lattice constraints,

then allowed the correct space group to be found during structure solution by *SHELXT*.

The unit cells of the four indexed data sets were highly consistent, shown in Table S3. This may be attributed to the lack of post-sample lenses and the precision of the goniometer of the ED-1 instrumental. We found that scan-varying refinement of the unit cells showed only small changes during each scan, with the greatest change being an increase of 0.1 Å in the c parameter of data set `07`. Merging statistics were no better using a scan-varying model for the cell as compared with allowing only the crystal orientation to vary smoothly with scan position. Therefore, we continued with this simpler model for each data set, by setting the option `crystal.unit_cell.force_static=True` for *dials.refine*.

4.1.3. Combining data sets, scaling and export

The integrated data sets were combined and a single unit cell was refined using this *dials.two_theta_refine* command, where the path to the parent directory containing processed data sets was stored in the variable `TPB_PROC`:
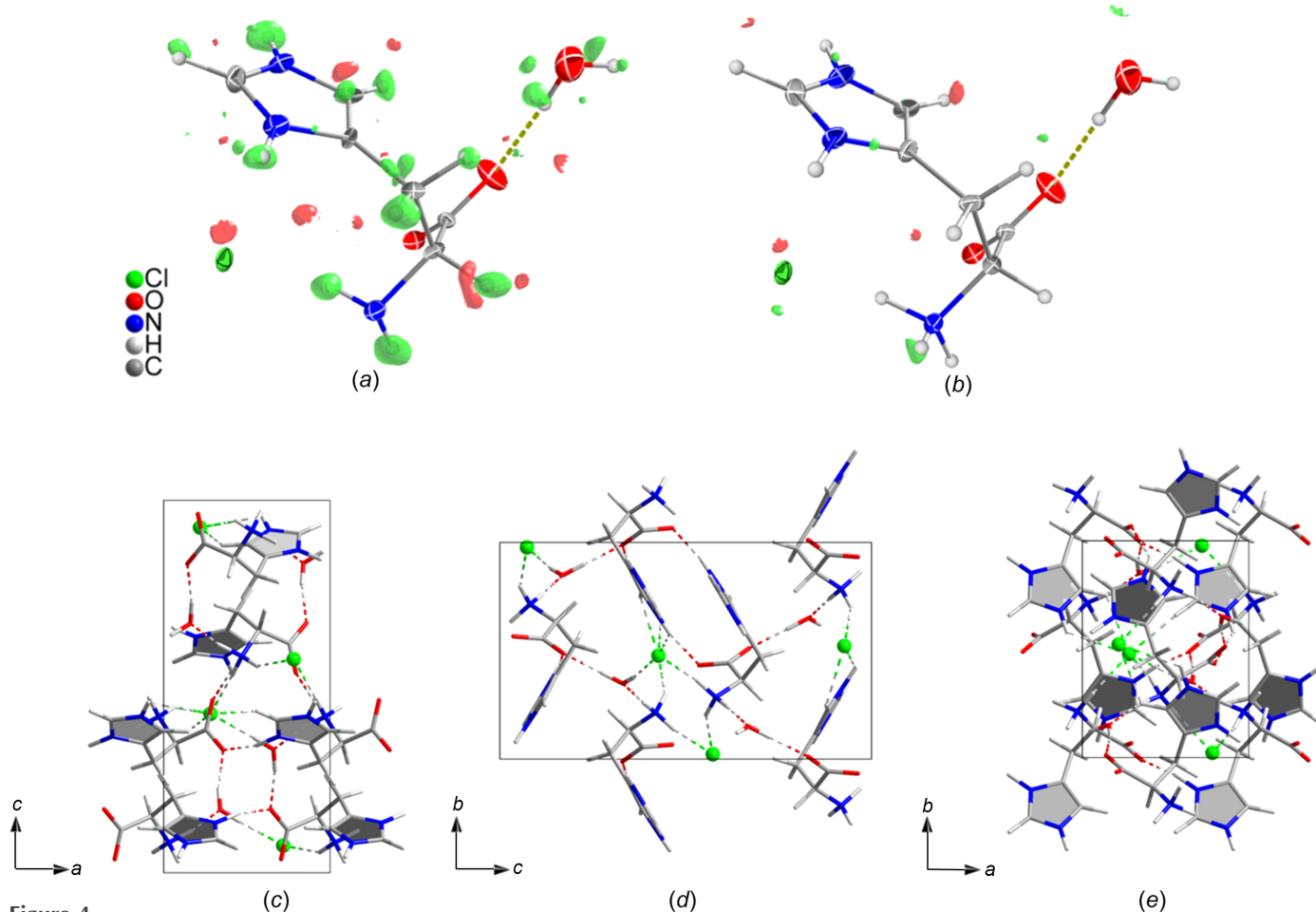

Figure 4
The structural model of L-histidine. An asymmetric unit superimposed with the $F_{obs}-F_{calc}$ map contoured at 3σ calculated (*a*) before any H atoms were added and (*b*) before adding the last H atom. H-atom positions were placed where they were expected to be based on the positive density peaks from the $F_{obs}-F_{calc}$ omit map. Positive peaks are shown in green and negative ones are shown in red. The structure model viewed along the (*c*) [100], (*d*) [010] and (*e*) [001] directions, showing the hydrogen-bond network.

Table 3
Statistics for joint scaling of four TPB data sets.

Crystallographic data and merging statistics			
Molecular formula	$C_{24}H_{18}$		
Space group	$Pna2_1$		
a, b, c (Å)	7.5894 (4), 11.2305 (4), 19.7150 (6)		
	Overall	Low	High
High resolution limit	0.75	1.61	0.75
Low resolution limit	9.86	9.86	0.78
Completeness (%)	99.3	98.6	96.8
Multiplicity	12.5	12.2	6.8
I/σ	5.5	20.9	0.4
$R_{meas}(I)$	0.230	0.140	1.541
$R_{pim}(I)$	0.061	0.039	0.564
$CC_{1/2}$	0.993	0.991	0.295
Total observations	29950	3388	1465
Total unique	2391	277	214
Kinematical refinement			
Reflections		All	$[I > 2\sigma(I)]$
Independent reflections		4137	1778
R_1		0.1685	0.1087
wR_2		0.2796	0.2511
Goof		0.889	

```
dials.two_theta_refine\
    "$TPB_PROC"/03/integrated.{expt,refl}\
    "$TPB_PROC"/06/integrated.{expt,refl}\
    "$TPB_PROC"/07/integrated.{expt,refl}\
    "$TPB_PROC"/08/integrated.{expt,refl}
```

The unit cell determined by this procedure was a = 7.5894 (4), b = 11.2305 (4) and c = 19.7150 (6) Å. Joint scaling and export of the four TPB data sets was achieved with these commands:

```
dials.scale refined_cell.expt\
    "$TPB_PROC"/03/integrated.refl\
```
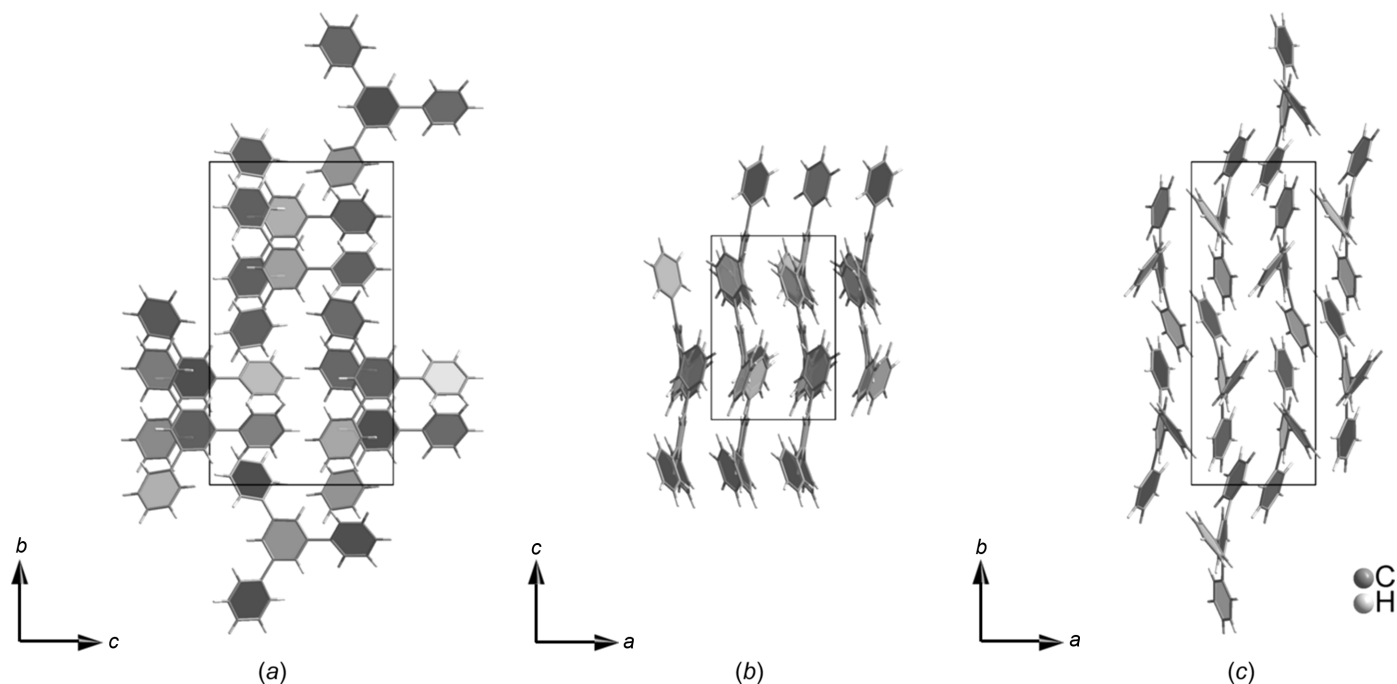
```
    "$TPB_PROC"/06/integrated.refl\
    "$TPB_PROC"/07/integrated.refl\
    "$TPB_PROC"/08/integrated.refl\
    d_min=0.75
dials.export scaled.expt scaled.refl\
    format=shelx composition="C H"
```

We explored the use of $\Delta CC_{1/2}$ filtering but found no advantage for these data sets. Merging statistics for this *dials.scale* run are given in Table 3.

4.2. Structure solution and refinement

Structure solution was performed, as with the natrolite and histidine examples, with *SHELXT*. Refinement was made using *SHELXL*. All non-H atoms were refined anisotropically with no restraints. H atoms were added in riding positions, and the extinction parameter EXTI was applied in the refinement. The structure is shown in Fig. 5.

5. Conclusions

The development of 3D ED has enhanced structure determination in chemical crystallography, enabling nano-crystallography from samples that previously could only be investigated by bulk *via* powder diffraction (Huang *et al.*, 2021; Gruene & Mugnaioli, 2021; Gemmi *et al.*, 2019). This technique has benefited over recent years from optimizations in instrumentation, data collection protocols and processing. In particular, the use of pixel array detectors for 3D ED applications has enabled rapid data collection free from readout noise. Fast data collection in turn facilitates the fine-sliced continuous rotation methodology that is the standard in X-ray

Figure 5
Projection of the TPB unit cell along the (*a*) [100], (*b*) [010] and (*c*) [001] directions.

crystallography. Data processing software used in X-ray crystallography is now a popular choice, as discounting the effect of post sample lenses, the effective diffraction geometry of the continuous rotation experiment is equivalent. Thus, the advances in data processing that improved data quality in X-ray crystallography, such as 3D profile fitting, may be applied to 3D ED data too.

DIALS is a popular package for single crystal data processing, under current active development. Recent additions to the *DIALS* package have improved its usability for 3D ED, so that it now provides a unified easily-scriptable framework for data processing across X-ray and electron diffraction. We demonstrate the use of *DIALS* for 3D ED of small molecule and framework structures with three examples from different instruments, with the common factor that data were recorded with a high-quality pixel array detector in each case. The first example shows how the software was adapted for data from an academic lab with a bespoke setup, in which regular calibration images were taken, interrupting the continuous sweep of diffraction data. The second and third examples come from commercial instruments, which we may expect to become increasingly important as the field matures. High quality data is achievable in each case. For the chiral amino acid L-histidine, we demonstrate how data processed with *DIALS* may be used for determining the absolute structure by emulating the output format used by *PETS2*, which is readable by *JANA2020* for dynamic diffraction-based refinement.

Future developments in *DIALS* for 3D ED should address some remaining deficiencies. For the Timepix and HyPix-ED detectors with a higher event multiplicity, or gain, the default spot-finding algorithm was found to be insensitive to weak spots. The gain was effectively halved for this step to increase sensitivity. Improvements to the spot-finding algorithm may be sought to make this adjustment unnecessary. The precise determination of unit-cell parameters is best demonstrated with the TPB data, where the lack of post-sample lenses on the Eldico ED-1 diffraction means there are no distortions introduced into the diffraction pattern. Comprehensive modelling of distortions has already been demonstrated (Brázda *et al.*, 2022), and this provides another obvious direction for improvements in *DIALS* for data collected on a TEM. Our experiences indicate that the standard method of error modelling developed for X-ray data typically underestimates the true error. Existing work to address this fact (Khouchen *et al.*, 2023) should inform developments in *DIALS*. We also found that the symmetry-determination tools in *DIALS* that can be used to resolve indexing ambiguities were not as effective with 3D ED data as they are with X-ray data, and their use is not demonstrated here. Work to improve the robustness of these tools will be important to simplify the workflow in cases in which the correct space group is not previously known.

DIALS is an open-source community project. The growing community of practitioners performing 3D ED includes methods developers, and we would like to make it clear that contributions from software developers interested in 3D ED are very welcome.

Data availability

The data sets described in this article are available to download on Zenodo. The direct links are: Natrolite, https://zenodo.org/records/12592764; Histidine, https://zenodo.org/records/10974780; TPB, https://zenodo.org/records/11119252. Data processing scripts for the examples presented here are made available on GitHub at https://github.com/aimeon/DIALS-proc. For the purpose of open access, the author has applied a Creative Commons Attribution (CC BY) licence to any Author Accepted Manuscript version arising.

References

Agirre, J., Atanasova, M., Bagdonas, H., Ballard, C. B., Baslé, A., Beilsten-Edmands, J., Borges, R. J., Brown, D. G., Burgos-Mármol, J. J., Berrisford, J. M., Bond, P. S., Caballero, I., Catapano, L., Chojnowski, G., Cook, A. G., Cowtan, K. D., Croll, T. I., Debreczeni, J. É., Devenish, N. E., Dodson, E. J., Drevon, T. R., Emsley, P., Evans, G., Evans, P. R., Fando, M., Foadi, J., Fuentes-Montero, L., Garman, E. F., Gerstel, M., Gildea, R. J., Hatti, K., Hekkelman, M. L., Heuser, P., Hoh, S. W., Hough, M. A., Jenkins, H. T., Jiménez, E., Joosten, R. P., Keegan, R. M., Keep, N., Krissinel, E. B., Kolenko, P., Kovalevskiy, O., Lamzin, V. S., Lawson, D. M., Lebedev, A. A., Leslie, A. G. W., Lohkamp, B., Long, F., Malý, M., McCoy, A. J., McNicholas, S. J., Medina, A., Millán, C., Murray, J. W., Murshudov, G. N., Nicholls, R. A., Noble, M. E. M., Oeffner, R., Pannu, N. S., Parkhurst, J. M., Pearce, N., Pereira, J., Perrakis, A., Powell, H. R., Read, R. J., Rigden, D. J., Rochira, W., Sammito, M., Sánchez Rodríguez, F., Sheldrick, G. M., Shelley, K. L., Simkovic, F.,

Simpkin, A. J., Skubak, P., Sobolev, E., Steiner, R. A., Stevenson, K., Tews, I., Thomas, J. M. H., Thorn, A., Valls, J. T., Uski, V., Usón, I., Vagin, A., Velankar, S., Vollmar, M., Walden, H., Waterman, D., Wilson, K. S., Winn, M. D., Winter, G., Wojdyr, M. & Yamashita, K. (2023). *Acta Cryst.* D**79**, 449–461.

Andrusenko, I. & Gemmi, M. (2022). *WIREs Nanomed. Nanobiotechnol.* **14**, e1810.

Artioli, G. & Galli, E. (1999). *Am. Mineral.* **84**, 1445–1450.

Beilsten-Edmands, J., Winter, G., Gildea, R., Parkhurst, J., Waterman, D. & Evans, G. (2020). *Acta Cryst.* D**76**, 385–399.

Brázda, P., Klementová, M., Krysiak, Y. & Palatinus, L. (2022). *IUCrJ*, **9**, 735–755.

Cho, J., Willhammar, T. & Zou, X. (2023). *Microporous Mesoporous Mater.* **358**, 112400.

Cichocka, M. O., Ångström, J., Wang, B., Zou, X. & Smeets, S. (2018). *J. Appl. Cryst.* **51**, 1652–1661.

Clabbers, M. T. B., Gruene, T., Parkhurst, J. M., Abrahams, J. P. & Waterman, D. G. (2018). *Acta Cryst.* D**74**, 506–518.

Clabbers, M. T. B. & Xu, H. (2021). *Acta Cryst.* D**77**, 313–324.

Evans, P. R. & Murshudov, G. N. (2013). *Acta Cryst.* D**69**, 1204–1214.

Fernandez-Perez, S., Boccone, V., Broennimann, C., Disch, C., Piazza, L., Radicci, V., Rissi, M., Schulze-Briese, C., Trueb, P. & Zambon, P. (2021). *J. Inst.* **16**, P10034.

Ge, M., Yang, T., Wang, Y., Carraro, F., Liang, W., Doonan, C., Falcaro, P., Zheng, H., Zou, X. & Huang, Z. (2021). *Faraday Discuss.* **231**, 66–80.

Gemmi, M., Mugnaioli, E., Gorelik, T. E., Kolb, U., Palatinus, L., Boullay, P., Hovmöller, S. & Abrahams, J. P. (2019). ACS Central Science, **5**, 1315–1329.

Gemmi, M., Palatinus, L., Klar, P., Faye, M., Agbemeh, V., Hajizadeh, A., Chintakindi, H., Suresh, A., Jeriga, B., Gemmrich Hernández, L., Santucci, M., Wang, L., Vypritskaia, A., Passuti, S., Cordero Oyonarte, E., Matinyan, S. & Ben Meriem, A. (2023). *Acta Cryst.* A**79**, C1085.

Genderen, E. van, Clabbers, M. T. B., Das, P. P., Stewart, A., Nederlof, I., Barentsen, K. C., Portillo, Q., Pannu, N. S., Nicolopoulos, S., Gruene, T. & Abrahams, J. P. (2016). *Acta Cryst.* A**72**, 236–242.

Gildea, R. J. & Winter, G. (2018). *Acta Cryst.* D**74**, 405–410.

Gruene, T., Clabbers, M. T. B., Luebben, J., Chin, J. M., Reithofer, M. R., Stowasser, F. & Alker, A. M. (2022). *J. Appl. Cryst.* **55**, 647–655.

Gruene, T. & Mugnaioli, E. (2021). *Chem. Rev.* **121**, 11823–11834.

Heidler, J., Pantelic, R., Wennmacher, J. T. C., Zaubitzer, C., Fecteau-Lefebvre, A., Goldie, K. N., Müller, E., Holstein, J. J., van Genderen, E., De Carlo, S. & Gruene, T. (2019). *Acta Cryst.* D**75**, 458–466.

Huang, Z., Willhammar, T. & Zou, X. (2021). *Chem. Sci.* **12**, 1206–1219.

Khouchen, M., Klar, P. B., Chintakindi, H., Suresh, A. & Palatinus, L. (2023). *Acta Cryst.* A**79**, 427–439.

Klar, P. B. (2023). jana_tools GitHub. https://github.com/pbklar/jana_tools.

Klar, P. B., Krysiak, Y., Xu, H., Steciuk, G., Cho, J., Zou, X. & Palatinus, L. (2023). *Nat. Chem.* **15**, 848–855.

Kolb, U., Gorelik, T. & Mugnaioli, E. (2009). *Mater. Res. Soc. Symp. Proc.* **1184**, 11–23.

Palatinus, L., Brázda, P., Jelínek, M., Hrdá, J., Steciuk, G. & Klementová, M. (2019). *Acta Cryst.* B**75**, 512–522.

Parkhurst, J. M., Brewster, A. S., Fuentes-Montero, L., Waterman, D. G., Hattne, J., Ashton, A. W., Echols, N., Evans, G., Sauter, N. K. & Winter, G. (2014). *J. Appl. Cryst.* **47**, 1459–1465.

Samperisi, L., Zou, X. & Huang, Z. (2022). *CrystEngComm*, **24**, 2719–2728.

Sheldrick, G. M. (2015a). *Acta Cryst.* C**71**, 3–8.

Sheldrick, G. M. (2015b). *Acta Cryst.* C**71**, 3–8.

Shi, D., Nannenga, B. L., Iadanza, M. G. & Gonen, T. (2013). *eLife*, **2**, e01345.

Simoncic, P., Romeijn, E., Hovestreydt, E., Steinfeld, G., Santiso-Quiñones, G. & Merkelbach, J. (2023). *Acta Cryst.* E**79**, 410–422.

Waterman, D. & Evans, G. (2010). *J. Appl. Cryst.* **43**, 1356–1371.

Waterman, D. G., Frisina, N., Owen, C. D., Winter, G. & Nunes, P. (2023). *Structure*, **31**, P1510–P1517.

Waterman, D. G., Winter, G., Gildea, R. J., Parkhurst, J. M., Brewster, A. S., Sauter, N. K. & Evans, G. (2016). *Acta Cryst.* D**72**, 558–575.

Winter, G., Waterman, D. G., Parkhurst, J. M., Brewster, A. S., Gildea, R. J., Gerstel, M., Fuentes-Montero, L., Vollmar, M., Michels-Clark, T., Young, I. D., Sauter, N. K. & Evans, G. (2018). *Acta Cryst.* D**74**, 85–97.

Xu, H., Lebrette, H., Yang, T., Srinivas, V., Hovmöller, S., Högbom, M. & Zou, X. (2018). *Structure*, **26**, 667–675.

supporting information

How to use *DIALS* to process chemical crystallography 3D ED rotation data from pixel array detectors

Angelina Vypritskaia, Xiaodong Zou, Taimin Yang and David Geoffrey Waterman

Computing details

(natrolite)

Crystal data

$Al_8H_{16}Na_8O_{48}Si_{12}$	$F(000) = 517$
$M_r = 1520.89$	$D_x = 2.111$ Mg m^{-3}
Orthorhombic, *Fdd*2	Electrons radiation, $\lambda = 0.0251$ Å
$a = 18.634$ (8) Å	Cell parameters from 2469 reflections
$b = 18.788$ (4) Å	$\theta = 0.1–1.2°$
$c = 6.8361$ (15) Å	$\mu = 0.000$ mm^{-1}
$V = 2393.3$ (13) Å^3	$T = 293$ K
$Z = 2$	Powder, white

Data collection

JEOL JEM-2100 TEM diffractometer	1948 reflections with $I > 2\sigma(I)$
Radiation source: LaB6	$R_{int} = 0.174$
3D ED scans	$\theta_{max} = 1.2°$, $\theta_{min} = 0.1°$
9890 measured reflections	$h = -27 \rightarrow 25$
2469 independent reflections	$k = -25 \rightarrow 30$
	$l = -10 \rightarrow 11$

Refinement

Refinement on F^2	$w = 1/[\sigma^2(F_o^2) + (0.1888P)^2 + 2.0409P]$
Least-squares matrix: full	where $P = (F_o^2 + 2F_c^2)/3$
$R[F^2 > 2\sigma(F^2)] = 0.139$	$(\Delta/\sigma)_{max} < 0.001$
$wR(F^2) = 0.379$	$\Delta\rho_{max} = 0.32$ e Å^{-3}
$S = 1.17$	$\Delta\rho_{min} = -0.25$ e Å^{-3}
2469 reflections	Extinction correction: SHELXL2019/2 (Sheldrick 2015*b*),
93 parameters	Fc*=kFc[1+0.001xFc$^2\lambda^3$/sin(2θ)]$^{-1/4}$
2 restraints	Extinction coefficient: 3358 (82)
Hydrogen site location: mixed	Absolute structure: All f″ are zero, so absolute structure could not be determined
H atoms treated by a mixture of independent and constrained refinement	

Special details

Geometry. All esds (except the esd in the dihedral angle between two l.s. planes) are estimated using the full covariance matrix. The cell esds are taken into account individually in the estimation of esds in distances, angles and torsion angles; correlations between esds in cell parameters are only used when they are defined by crystal symmetry. An approximate (isotropic) treatment of cell esds is used for estimating esds involving l.s. planes.

Fractional atomic coordinates and isotropic or equivalent isotropic displacement parameters (Å²)

	x	*y*	*z*	U_{iso}*/U_{eq}
Si01	0.3464 (3)	0.7117 (2)	0.1828 (7)	0.0120 (8)
Na1	0.2791 (5)	0.5315 (4)	0.1912 (14)	0.0303 (15)
Si02	0.250000	0.750000	0.5547 (9)	0.0134 (11)
Al03	0.2870 (3)	0.8438 (2)	0.9418 (7)	0.0131 (9)
O005	0.4298 (4)	0.6816 (4)	0.1979 (11)	0.0156 (12)
O006	0.3474 (5)	0.7860 (4)	0.0575 (14)	0.0233 (16)
O007	0.2934 (5)	0.6531 (5)	0.0824 (13)	0.0228 (16)
O008	0.3200 (5)	0.7279 (5)	0.4148 (10)	0.0203 (15)
O009	0.2728 (5)	0.8174 (4)	0.6949 (12)	0.0213 (14)
O00A	0.1930 (6)	0.5602 (6)	0.4460 (18)	0.035 (2)
H1A	0.1440 (15)	0.557 (4)	0.393 (4)	0.052*
H1B	0.195 (5)	0.606 (5)	0.529 (13)	0.052*

Atomic displacement parameters (Å²)

	U^{11}	U^{22}	U^{33}	U^{12}	U^{13}	U^{23}
Si01	0.012 (2)	0.0095 (15)	0.0139 (16)	0.0009 (13)	−0.0002 (15)	0.0023 (15)
Na1	0.030 (4)	0.021 (3)	0.040 (4)	0.000 (2)	−0.006 (3)	0.008 (3)
Si02	0.011 (3)	0.015 (3)	0.014 (2)	−0.002 (2)	0.000	0.000
Al03	0.015 (2)	0.0107 (17)	0.0137 (17)	−0.0019 (14)	0.0030 (17)	−0.0048 (16)
O005	0.015 (3)	0.014 (3)	0.018 (3)	0.002 (2)	−0.004 (3)	−0.002 (2)
O006	0.026 (4)	0.014 (3)	0.030 (4)	0.007 (3)	−0.006 (3)	0.006 (3)
O007	0.017 (4)	0.021 (3)	0.029 (4)	−0.001 (3)	−0.012 (3)	0.003 (3)
O008	0.020 (4)	0.029 (4)	0.012 (3)	−0.002 (3)	0.004 (2)	0.001 (3)
O009	0.020 (4)	0.023 (3)	0.021 (3)	−0.002 (3)	−0.003 (3)	−0.007 (3)
O00A	0.031 (5)	0.038 (5)	0.034 (4)	0.001 (4)	0.001 (4)	0.009 (4)

Geometric parameters (Å, º)

Si01—O007	1.630 (9)	Na1—Al03[v]	3.148 (9)
Si01—O006	1.639 (9)	Si02—O009	1.644 (8)
Si01—O005	1.658 (9)	Si02—O009[vi]	1.644 (8)
Si01—O008	1.687 (8)	Si02—O008[vi]	1.671 (9)
Si01—Na1[i]	3.136 (9)	Si02—O008	1.671 (9)
Na1—O007	2.416 (11)	Al03—O006[vii]	1.752 (9)
Na1—O00A	2.429 (16)	Al03—O005[viii]	1.762 (8)
Na1—O006[ii]	2.436 (13)	Al03—O009	1.779 (9)
Na1—O00A[iii]	2.459 (14)	Al03—O007[ix]	1.782 (9)
Na1—O005[iv]	2.582 (11)		
O007—Si01—O006	111.2 (5)	Si01[ii]—Na1—Al03[v]	152.4 (3)
O007—Si01—O005	111.3 (5)	O009—Si02—O009[vi]	108.7 (7)
O006—Si01—O005	108.2 (5)	O009—Si02—O008[vi]	110.1 (4)
O007—Si01—O008	110.0 (5)	O009[vi]—Si02—O008[vi]	108.9 (4)
O006—Si01—O008	110.0 (5)	O009—Si02—O008	108.9 (4)

O005—Si01—O008	106.0 (5)	O009^{vi}—Si02—O008	110.1 (4)

O005—Si01—O008	106.0 (5)	O009[vi]—Si02—O008	110.1 (4)
O007—Si01—Na1[i]	120.6 (4)	O008[vi]—Si02—O008	110.1 (6)
O006—Si01—Na1[i]	50.2 (4)	O006[vii]—Al03—O005[viii]	110.2 (5)
O005—Si01—Na1[i]	58.7 (3)	O006[vii]—Al03—O009	110.5 (5)
O008—Si01—Na1[i]	129.4 (4)	O005[viii]—Al03—O009	109.6 (5)
O007—Na1—O00A	94.8 (4)	O006[vii]—Al03—O007[ix]	108.5 (5)
O007—Na1—O006[ii]	87.9 (4)	O005[viii]—Al03—O007[ix]	104.6 (4)
O00A—Na1—O006[ii]	112.5 (5)	O009—Al03—O007[ix]	113.3 (5)
O007—Na1—O00A[iii]	115.4 (5)	O006[vii]—Al03—Na1[ix]	117.9 (4)
O00A—Na1—O00A[iii]	141.6 (4)	O005[viii]—Al03—Na1[ix]	55.1 (3)
O006[ii]—Na1—O00A[iii]	92.7 (4)	O009—Al03—Na1[ix]	131.5 (4)
O007—Na1—O005[iv]	68.1 (3)	O007[ix]—Al03—Na1[ix]	49.8 (3)
O00A—Na1—O005[iv]	85.9 (4)	Si01—O005—Al03[x]	130.2 (5)
O006[ii]—Na1—O005[iv]	151.4 (4)	Si01—O005—Na1[xi]	128.4 (4)
O00A[iii]—Na1—O005[iv]	84.3 (4)	Al03[x]—O005—Na1[xi]	90.9 (4)
O007—Na1—Si01[ii]	118.4 (4)	Si01—O006—Al03[xii]	139.2 (7)
O00A—Na1—Si01[ii]	101.8 (4)	Si01—O006—Na1[i]	98.7 (4)
O006[ii]—Na1—Si01[ii]	31.1 (2)	Al03[xii]—O006—Na1[i]	118.7 (5)
O00A[iii]—Na1—Si01[ii]	84.8 (4)	Si01—O007—Al03[v]	135.6 (6)
O005[iv]—Na1—Si01[ii]	169.0 (4)	Si01—O007—Na1	125.1 (5)
O007—Na1—Al03[v]	34.3 (2)	Al03[v]—O007—Na1	96.0 (4)
O00A—Na1—Al03[v]	88.0 (4)	Si02—O008—Si01	144.1 (6)
O006[ii]—Na1—Al03[v]	121.4 (3)	Si02—O009—Al03	143.7 (6)
O00A[iii]—Na1—Al03[v]	103.6 (4)	Na1—O00A—Na1[xiii]	101.2 (4)
O005[iv]—Na1—Al03[v]	34.0 (2)		

Symmetry codes: (i) −x+3/4, y+1/4, z−1/4; (ii) −x+3/4, y−1/4, z+1/4; (iii) −x+1/2, −y+1, z−1/2; (iv) x−1/4, −y+5/4, z−1/4; (v) −x+1/2, −y+3/2, z−1; (vi) −x+1/2, −y+3/2, z; (vii) x, y, z+1; (viii) −x+3/4, y+1/4, z+3/4; (ix) −x+1/2, −y+3/2, z+1; (x) −x+3/4, y−1/4, z−3/4; (xi) x+1/4, −y+5/4, z+1/4; (xii) x, y, z−1; (xiii) −x+1/2, −y+1, z+1/2.

(histidine)

Crystal data

$C_6H_{10}N_3O_2^+ \cdot Cl^- \cdot H_2O$
$M_r = 209.64$
Orthorhombic, $P2_12_12_1$
$a = 6.7936 (3)$ Å
$b = 8.8294 (4)$ Å
$c = 15.1621 (10)$ Å
$V = 909.47 (8)$ Å^3
$Z = 4$

$F(000) = 155$
$D_x = 1.531$ Mg m^{-3}
Electrons radiation, $\lambda = 0.0251$ Å
Cell parameters from 3641 reflections
$\theta = 0.1–1.1°$
$\mu = 0.000$ mm^{-1}
$T = 293$ K
Powder, white

Data collection

Rigaku XtaLAB Synergy-ED
    diffractometer
Radiation source: JEOL JSM-2300ED
3D ED scans
85165 measured reflections
3641 independent reflections

2589 reflections with $I > 2\sigma(I)$
$R_{int} = 0.425$
$\theta_{max} = 1.1°$, $\theta_{min} = 0.1°$
$h = -10 \rightarrow 10$
$k = -13 \rightarrow 13$
$l = -23 \rightarrow 23$

Refinement

Refinement on F^2	$w = 1/[\sigma^2(F_o^2) + (0.1315P)^2 + 0.1548P]$
Least-squares matrix: full	where $P = (F_o^2 + 2F_c^2)/3$
$R[F^2 > 2\sigma(F^2)] = 0.123$	$(\Delta/\sigma)_{max} = 0.060$
$wR(F^2) = 0.322$	$\Delta\rho_{max} = 0.18$ e Å^{-3}
$S = 1.12$	$\Delta\rho_{min} = -0.19$ e Å^{-3}
3641 reflections	Extinction correction: SHELXL2019/2
167 parameters	(Sheldrick 2015*b*),
1 restraint	$Fc^* = kFc[1 + 0.001 x Fc^2\lambda^3/\sin(2\theta)]^{-1/4}$
Hydrogen site location: difference Fourier map	Extinction coefficient: 9000 (16)
All H-atom parameters refined	Absolute structure: All f″ are zero, so absolute structure could not be determined

Special details

Geometry. All esds (except the esd in the dihedral angle between two l.s. planes) are estimated using the full covariance matrix. The cell esds are taken into account individually in the estimation of esds in distances, angles and torsion angles; correlations between esds in cell parameters are only used when they are defined by crystal symmetry. An approximate (isotropic) treatment of cell esds is used for estimating esds involving l.s. planes.

Fractional atomic coordinates and isotropic or equivalent isotropic displacement parameters (Å²)

	x	*y*	*z*	U_{iso}*/U_{eq}
Cl1	0.2817 (4)	0.4777 (3)	0.4269 (2)	0.0196 (7)
O1	0.8578 (8)	0.5116 (8)	0.6705 (5)	0.0314 (16)
O2	0.7942 (8)	0.4333 (6)	0.5365 (4)	0.0207 (11)
C1	0.7555 (8)	0.4440 (7)	0.6157 (5)	0.0142 (13)
C2	0.5738 (9)	0.3657 (7)	0.6517 (5)	0.0146 (12)
H2	0.607 (8)	0.277 (6)	0.704 (4)	0.045 (11)*
N1	0.4699 (8)	0.2857 (6)	0.5811 (4)	0.0157 (11)
H1A	0.413 (5)	0.363 (4)	0.531 (2)	0.023 (7)*
H1B	0.562 (4)	0.204 (4)	0.555 (2)	0.018 (6)*
H1C	0.333 (5)	0.242 (5)	0.612 (3)	0.041 (10)*
C4	0.4402 (10)	0.4731 (7)	0.7016 (5)	0.0177 (13)
H4A	0.524 (6)	0.503 (5)	0.761 (3)	0.038 (10)*
H4B	0.314 (5)	0.416 (4)	0.719 (2)	0.022 (7)*
C5	0.3822 (9)	0.6121 (7)	0.6520 (5)	0.0157 (13)
N5	0.1917 (8)	0.6488 (6)	0.6339 (4)	0.0176 (12)
H5	0.059 (5)	0.579 (4)	0.658 (3)	0.024 (7)*
C6	0.1848 (9)	0.7748 (8)	0.5897 (5)	0.0212 (15)
H6	0.063 (6)	0.843 (5)	0.566 (3)	0.033 (8)*
N7	0.3655 (10)	0.8235 (7)	0.5804 (5)	0.0237 (13)
H7	0.408 (6)	0.920 (5)	0.543 (3)	0.033 (8)*
C8	0.4922 (9)	0.7262 (7)	0.6181 (5)	0.0191 (14)
H8	0.645 (4)	0.750 (3)	0.621 (2)	0.017 (6)*
O3	0.8396 (10)	0.6514 (9)	0.8312 (5)	0.0374 (17)
H3A	0.952 (6)	0.622 (4)	0.861 (3)	0.030 (8)*
H3B	0.831 (5)	0.602 (4)	0.775 (3)	0.025 (7)*

Atomic displacement parameters (Å²)

	U^{11}	U^{22}	U^{33}	U^{12}	U^{13}	U^{23}
Cl1	0.0119 (10)	0.0187 (13)	0.0282 (18)	−0.0005 (10)	−0.0027 (11)	0.0058 (13)
O1	0.0105 (19)	0.055 (4)	0.029 (4)	−0.010 (2)	0.003 (2)	−0.014 (3)
O2	0.019 (2)	0.018 (2)	0.025 (3)	−0.0012 (19)	0.004 (2)	0.003 (2)
C1	0.009 (2)	0.013 (3)	0.020 (4)	0.0008 (18)	−0.002 (2)	−0.002 (3)
C2	0.015 (2)	0.013 (3)	0.016 (3)	−0.002 (2)	−0.002 (2)	0.000 (3)
N1	0.016 (2)	0.014 (2)	0.017 (3)	0.0027 (18)	−0.001 (2)	0.001 (2)
C4	0.027 (3)	0.008 (3)	0.018 (3)	0.000 (2)	0.000 (3)	0.000 (2)
C5	0.013 (2)	0.013 (3)	0.021 (4)	0.000 (2)	−0.001 (2)	0.004 (3)
N5	0.014 (2)	0.014 (2)	0.024 (3)	0.0001 (18)	0.002 (2)	0.004 (2)
C6	0.009 (2)	0.024 (3)	0.030 (4)	0.003 (2)	−0.005 (2)	−0.002 (3)
N7	0.030 (3)	0.012 (2)	0.029 (4)	0.003 (2)	0.003 (3)	0.005 (3)
C8	0.014 (2)	0.013 (3)	0.031 (4)	−0.003 (2)	0.004 (3)	0.002 (3)
O3	0.031 (3)	0.052 (4)	0.029 (4)	0.021 (3)	−0.005 (3)	−0.008 (4)

Geometric parameters (Å, º)

O1—C1	1.236 (9)	C5—C8	1.355 (9)
O2—C1	1.233 (9)	C5—N5	1.362 (8)
C1—C2	1.516 (9)	N5—C6	1.300 (9)
C2—N1	1.464 (9)	C6—N7	1.309 (9)
C2—C4	1.515 (9)	N7—C8	1.343 (9)
C4—C5	1.492 (9)		
O2—C1—O1	124.9 (6)	C8—C5—N5	105.7 (6)
O2—C1—C2	119.2 (6)	C8—C5—C4	131.0 (6)
O1—C1—C2	115.8 (6)	N5—C5—C4	123.2 (6)
N1—C2—C4	112.2 (5)	C6—N5—C5	110.0 (5)
N1—C2—C1	110.5 (6)	N5—C6—N7	107.6 (6)
C4—C2—C1	112.5 (5)	C6—N7—C8	110.2 (6)
C5—C4—C2	114.9 (6)	N7—C8—C5	106.5 (6)

(tpb)

Crystal data

C$_{24}$H$_{18}$
$M_r = 306.41$
Orthorhombic, $Pna2_1$
$a = 7.5893$ (4) Å
$b = 19.7154$ (6) Å
$c = 11.2305$ (4) Å
$V = 1680.38$ (12) Å³
$Z = 4$

$F(000) = 279$
$D_x = 1.211$ Mg m⁻³
Electrons radiation, $\lambda = 0.02851$ Å
Cell parameters from 4137 reflections
$\theta = 0.1–1.1°$
$\mu = 0.000$ mm⁻¹
$T = 293$ K
Powder, white

Data collection

Eldico ED-1 diffractometer	1778 reflections with $I > 2\sigma(I)$
Radiation source: LaB6	$R_{int} = 0.213$
3D ED scans	$\theta_{max} = 1.1°$, $\theta_{min} = 0.1°$
28267 measured reflections	$h = -10 \rightarrow 10$
4137 independent reflections	$k = -26 \rightarrow 26$
	$l = -14 \rightarrow 14$

Refinement

Refinement on F^2	$w = 1/[\sigma^2(F_o^2) + (0.1515P)^2]$
Least-squares matrix: full	where $P = (F_o^2 + 2F_c^2)/3$
$R[F^2 > 2\sigma(F^2)] = 0.109$	$(\Delta/\sigma)_{max} < 0.001$
$wR(F^2) = 0.280$	$\Delta\rho_{max} = 0.14$ e Å^{-3}
$S = 0.89$	$\Delta\rho_{min} = -0.13$ e Å^{-3}
4137 reflections	Extinction correction: SHELXL2019/2
218 parameters	(Sheldrick, 2015b),
1 restraint	Fc*=kFc[1+0.001xFc$^2\lambda^3$/sin(2θ)]$^{-1/4}$
Hydrogen site location: inferred from	Extinction coefficient: 3621 (22)
neighbouring sites	Absolute structure: All f'' are zero, so absolute
H-atom parameters constrained	structure could not be determined

Special details

Geometry. All esds (except the esd in the dihedral angle between two l.s. planes) are estimated using the full covariance matrix. The cell esds are taken into account individually in the estimation of esds in distances, angles and torsion angles; correlations between esds in cell parameters are only used when they are defined by crystal symmetry. An approximate (isotropic) treatment of cell esds is used for estimating esds involving l.s. planes.

Fractional atomic coordinates and isotropic or equivalent isotropic displacement parameters (Å^2)

	x	y	z	U_{iso}*/U_{eq}
C001	0.7767 (11)	0.6076 (3)	0.3482 (6)	0.0310 (19)
C002	0.7545 (12)	0.7194 (4)	0.7358 (7)	0.038 (2)
H002	0.826407	0.753000	0.703891	0.045*
C003	0.7159 (10)	0.6695 (3)	0.5338 (6)	0.0292 (17)
C004	0.7512 (11)	0.7312 (3)	0.3482 (7)	0.0348 (19)
C005	0.7188 (13)	0.7306 (3)	0.4698 (7)	0.039 (2)
H005	0.698807	0.771290	0.509484	0.046*
C006	0.6872 (14)	0.7992 (4)	0.1649 (7)	0.050 (2)
H006	0.644799	0.759998	0.128960	0.060*
C007	0.7807 (11)	0.6707 (3)	0.2883 (7)	0.038 (2)
H007	0.803541	0.671652	0.207006	0.046*
C008	0.8168 (11)	0.5461 (3)	0.2878 (7)	0.038 (2)
C009	0.5803 (13)	0.6186 (4)	0.7121 (7)	0.044 (2)
H009	0.539121	0.583426	0.664493	0.053*
C00A	0.9123 (12)	0.4917 (3)	0.3409 (8)	0.043 (2)
H00A	0.952625	0.496013	0.418769	0.052*
C00B	0.7500 (12)	0.6099 (3)	0.4713 (7)	0.036 (2)
H00B	0.755303	0.569505	0.513796	0.044*
C00C	0.6089 (14)	0.6683 (4)	0.9053 (8)	0.057 (3)
H00C	0.581957	0.668296	0.986042	0.068*
C00D	0.6810 (11)	0.6697 (3)	0.6612 (7)	0.0352 (18)

C00E	0.8020 (15)	0.4736 (4)	0.1123 (9)	0.062 (3)
H00E	0.768388	0.468046	0.033249	0.075*
C00F	0.5403 (14)	0.6189 (4)	0.8313 (8)	0.053 (2)
H00F	0.466499	0.585666	0.862410	0.064*
C00G	0.7196 (16)	0.7184 (4)	0.8575 (7)	0.058 (3)
H00G	0.769599	0.750931	0.907079	0.070*
C00H	0.7500 (11)	0.7961 (3)	0.2791 (7)	0.0359 (19)
C00I	0.8878 (12)	0.4239 (4)	0.1630 (10)	0.056 (2)
H00I	0.909765	0.383469	0.122865	0.067*
C00J	0.7570 (13)	0.5348 (4)	0.1689 (7)	0.049 (2)
H00J	0.689631	0.567315	0.129711	0.059*
C00K	0.8191 (14)	0.8552 (4)	0.3281 (8)	0.051 (2)
H00K	0.868890	0.853770	0.403669	0.061*
C00L	0.8155 (13)	0.9153 (4)	0.2679 (9)	0.056 (3)
H00L	0.854048	0.954724	0.305295	0.067*
C00M	0.7552 (15)	0.9181 (4)	0.1522 (9)	0.067 (3)
H00M	0.761154	0.958320	0.109005	0.080*
C00N	0.6855 (16)	0.8598 (4)	0.1014 (9)	0.069 (3)
H00N	0.637869	0.861180	0.025154	0.082*
C00O	0.9453 (14)	0.4339 (3)	0.2803 (9)	0.060 (3)
H00O	1.008405	0.399542	0.317710	0.072*

Atomic displacement parameters (Å²)

	U^{11}	U^{22}	U^{33}	U^{12}	U^{13}	U^{23}
C001	0.041 (6)	0.018 (3)	0.034 (5)	0.005 (3)	0.016 (3)	−0.001 (3)
C002	0.041 (6)	0.030 (4)	0.043 (5)	−0.014 (4)	0.010 (4)	−0.005 (3)
C003	0.036 (5)	0.022 (3)	0.029 (4)	0.001 (3)	0.001 (3)	−0.002 (3)
C004	0.040 (5)	0.023 (4)	0.041 (5)	0.008 (3)	0.005 (4)	0.004 (3)
C005	0.049 (7)	0.022 (4)	0.045 (5)	0.007 (3)	0.007 (4)	−0.008 (3)
C006	0.085 (8)	0.041 (4)	0.026 (4)	−0.005 (4)	0.005 (5)	0.003 (4)
C007	0.054 (7)	0.034 (4)	0.026 (4)	−0.007 (3)	0.014 (4)	0.003 (3)
C008	0.053 (6)	0.024 (3)	0.038 (4)	−0.001 (3)	−0.005 (4)	−0.011 (3)
C009	0.046 (7)	0.044 (5)	0.043 (5)	−0.019 (4)	0.004 (4)	0.001 (3)
C00A	0.049 (6)	0.028 (4)	0.052 (5)	0.017 (3)	−0.002 (4)	−0.003 (3)
C00B	0.047 (6)	0.020 (3)	0.042 (5)	0.004 (3)	0.001 (4)	0.001 (3)
C00C	0.083 (9)	0.061 (6)	0.027 (5)	0.004 (5)	0.011 (5)	−0.009 (4)
C00D	0.049 (6)	0.026 (3)	0.030 (4)	0.002 (3)	−0.013 (4)	−0.005 (3)
C00E	0.081 (9)	0.058 (5)	0.047 (6)	−0.023 (5)	0.014 (5)	−0.031 (5)
C00F	0.061 (7)	0.047 (5)	0.051 (6)	−0.009 (4)	0.012 (5)	0.000 (4)
C00G	0.088 (10)	0.050 (5)	0.037 (5)	−0.007 (5)	−0.001 (5)	−0.014 (4)
C00H	0.047 (6)	0.024 (3)	0.037 (4)	−0.006 (3)	0.008 (4)	0.002 (3)
C00I	0.051 (6)	0.037 (4)	0.079 (7)	0.006 (4)	0.007 (6)	−0.019 (5)
C00J	0.075 (7)	0.033 (4)	0.038 (5)	−0.004 (4)	−0.011 (5)	−0.006 (4)
C00K	0.061 (7)	0.040 (4)	0.051 (5)	−0.008 (4)	−0.008 (5)	0.013 (4)
C00L	0.059 (8)	0.026 (4)	0.082 (7)	−0.001 (4)	0.006 (5)	0.013 (4)
C00M	0.106 (9)	0.038 (5)	0.057 (6)	0.016 (5)	0.019 (6)	0.027 (4)
C00N	0.105 (9)	0.059 (5)	0.042 (5)	0.036 (6)	−0.005 (6)	0.006 (5)

C00O	0.074 (8)	0.025 (4)	0.080 (7)	0.006 (4)	0.030 (6)	−0.006 (4)

Geometric parameters (Å, º)

C001—C00B	1.399 (10)	C008—C00J	1.428 (11)
C001—C007	1.413 (9)	C009—C00F	1.372 (11)
C001—C008	1.423 (9)	C009—C00D	1.388 (10)
C002—C00G	1.392 (11)	C00A—C00O	1.350 (10)
C002—C00D	1.405 (10)	C00C—C00F	1.382 (12)
C003—C00B	1.392 (9)	C00C—C00G	1.404 (13)
C003—C005	1.402 (10)	C00E—C00I	1.307 (13)
C003—C00D	1.455 (11)	C00E—C00J	1.407 (11)
C004—C005	1.388 (10)	C00H—C00K	1.392 (11)
C004—C007	1.388 (9)	C00I—C00O	1.402 (14)
C004—C00H	1.495 (9)	C00K—C00L	1.364 (10)
C006—C00H	1.370 (11)	C00L—C00M	1.379 (14)
C006—C00N	1.390 (11)	C00M—C00N	1.389 (14)
C008—C00A	1.426 (10)		
C00B—C001—C007	116.4 (6)	C003—C00B—C001	123.5 (7)
C00B—C001—C008	122.0 (6)	C00F—C00C—C00G	119.5 (8)
C007—C001—C008	121.3 (6)	C009—C00D—C002	118.6 (7)
C00G—C002—C00D	120.0 (8)	C009—C00D—C003	120.2 (7)
C00B—C003—C005	117.6 (7)	C002—C00D—C003	121.1 (7)
C00B—C003—C00D	122.1 (6)	C00I—C00E—C00J	124.6 (9)
C005—C003—C00D	120.3 (6)	C009—C00F—C00C	120.4 (9)
C005—C004—C007	119.8 (6)	C002—C00G—C00C	119.9 (8)
C005—C004—C00H	121.1 (6)	C006—C00H—C00K	117.5 (7)
C007—C004—C00H	119.0 (7)	C006—C00H—C004	121.8 (7)
C004—C005—C003	121.0 (6)	C00K—C00H—C004	120.6 (7)
C00H—C006—C00N	121.5 (8)	C00E—C00I—C00O	117.3 (8)
C004—C007—C001	121.5 (7)	C00E—C00J—C008	118.6 (8)
C001—C008—C00A	123.5 (7)	C00L—C00K—C00H	121.7 (8)
C001—C008—C00J	120.6 (7)	C00K—C00L—C00M	120.5 (8)
C00A—C008—C00J	115.9 (6)	C00L—C00M—C00N	118.7 (8)
C00F—C009—C00D	121.4 (8)	C00M—C00N—C006	119.8 (10)
C00O—C00A—C008	121.2 (9)	C00A—C00O—C00I	122.4 (9)